Hindawi
Advances in Civil Engineering
Volume 2022, Article ID 3056668, 22 pages
https://doi.org/10.1155/2022/3056668

Research Article

Mechanical Behavior of Loess Tunnels Caused by Surface Water Joints Infiltration

Qingfu Li, Ming Liu, and Yingqiao Yu

School of Water Conservancy Engineering, Zhengzhou University, Zhengzhou 450003, China

Correspondence should be addressed to Ming Liu; lmxiaoyu@gs.zzu.edu.cn

Received 26 December 2021; Revised 9 May 2022; Accepted 12 May 2022; Published 30 May 2022

Academic Editor: Zhijun Xu

Many researchers have conducted a vast amount of research on water sensitivity and joint seepage in loess tunnels. However, studies on the mechanical effects of shallow buried loess tunnels under the influence of joint dominant seepage are still insufficient. In this study, we simulate the seepage range of loess tunnels with joints, and we use this seepage range to numerically simulate the mechanical properties of shallow buried loess tunnels. Studies have shown that the permeability coefficient and the number of joints are the key factors that affect the amount of surface water infiltration. An increase in the permeability coefficient on the order of 5×10^{-3} m/s will cause the surface water to pour into the ground and rapidly form a saturated soak zone on the liner, while an increase in the number of joints will increase the width and formation rate of the saturated zone. The results of the tunnel mechanics simulation show that the surface settlement and the surrounding rock displacement increase with the increase of the wetted area of the vault; the effect of arch footing water immersion on the surface settlement and the surrounding rock displacement is most significant for the same wetted area width. Compared with the three-stage method, the center cross diaphragm (CRD) method of excavation can better control the surface and the surrounding rock settlement under waterlogged conditions. In particular, the lining settlement on the waterlogged side can be effectively controlled, and the overall settlement of the tunnel is more uniform.

1. Introduction

Loess is a loose-packed powder soil formed in the Quaternary period, and it is widely distributed in arid and semiarid areas [1]. Loess deposits cover $6.5 \times 10^4 \text{km}^2$ in China, of which about $4 \times 10^4 \text{km}^2$ is collapsible loess [2]. The Q_3 and Q_4 loess formed in Upper Pleistocene and Holocene has the characteristics of no layering as well as loose texture and pore development. The unique metastable structure of loess will be destabilized and collapsed into small micropores when this soil is influenced by rain seepage, which is macroscopically manifested as a sudden decrease in strength and a large deformation after water immersion [3, 4]. The special metastable structure of collapsible loess is prone to collapse and large deformation beyond the normal level under the influence of construction disturbance and moisture immersion [5]. Self-weight wet-submerged loess surrounding rock in the immersion of water after a significant drop in strength produces a large deformation. Additionally, the self-supporting capacity of the surrounding rock is greatly reduced, and the stress redistribution caused by uneven settlement and the bias effect causes the tunnel lining to be in an unfavorable state of stress or even damage [6].

Loess joints are fracture gaps in the loess for which the soil is not significantly displaced along both sides of the fractures. Loess joints are with a certain degree of open fissures; during the surface rainwater infiltration, loess joints especially through the joints can often form the advantage of surface water infiltration channel [7]. Under the condition of high intensity infiltration of surface water, water will preferentially infiltrate along the dominant infiltration channels such as joint fissures, and the infiltration volume is extremely high, sometimes even up to 20 times of the infiltration volume in the uniform infiltration stage [8]. In the initial stage of the high intensity infiltration of surface water,

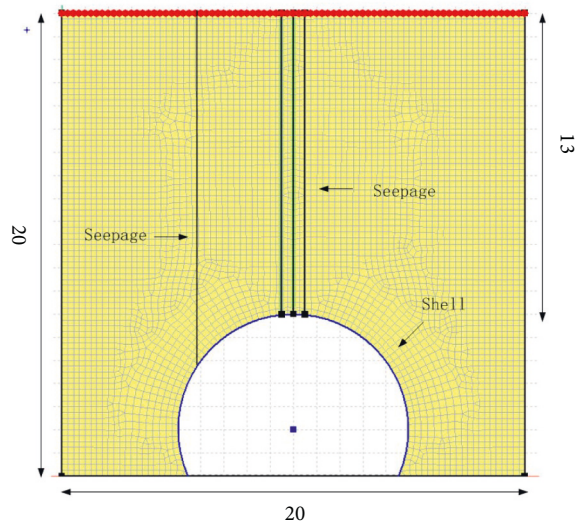

Figure 1: Model of loess joint seepage.

Table 1: Working condition setting of loess joint seepage.

Case	Location of the joints	Number of joints	Permeability coefficient of joints
Case 1	Vault	1	2×10^{-3} m/s
Case 2	Vault	2	2×10^{-3} m/s
Case 3	Vault	3	2×10^{-3} m/s
Case 4	Vault	1	5×10^{-3} m/s
Case 5	Arch shoulder	1	5×10^{-3} m/s

the tunnel perimeter rock will undergo severe uneven waterlogging, and the strength and deformation of the waterlogged loess perimeter rock will increase dramatically, resulting in stress redistribution and reduced self-supporting capacity within the perimeter rock, which will in turn lead to increased stress or bias pressure on the tunnel lining, deteriorating the mechanical properties of the lining and leaving the lining in a stress-unfriendly state. The lining stress behavior is very different from that of the perimeter rock before the wetting [9–14]. Due to the ultrahigh water head, water leakage through tunnel joints is a major concern during a tunnel's service life [15]. Segmental joints are vulnerable parts of the lining structure in precast shield tunnels, from both the structural (lower stiffness compared to main segments) and nonstructural (potential water leakage points) perspectives [16, 17]. Segmental joints act as a weak link in the tunnel lining in terms of both structural responses (due to the lower stiffness and strength compared to the main segments) and the serviceability considerations (high risk of water/gas leakage) [18]. Water leakage through segmental joints is a clutch issue for shield tunnels during both the construction and operation stages [19, 20]. For a modern underwater tunnel subjected to high water head, the segments are required to cast by the high-performance concrete with excellent quality and very low permeability [21].

The mechanical properties of loess are very different under dry and wet conditions [22, 23]. Therefore, the study of the lining force characteristics of shallow buried loess

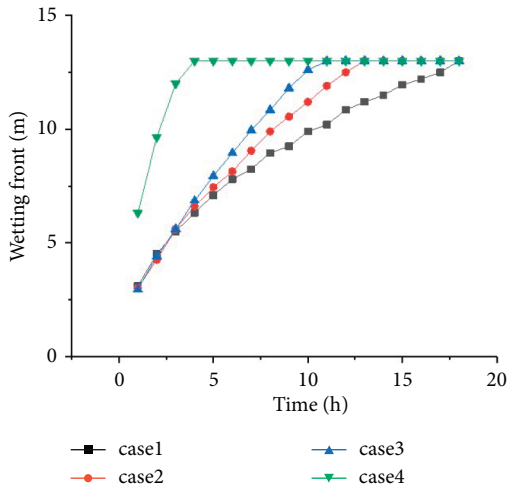

Figure 2: 24% wetting front depths of Case 1, Case 2, Case 3, and Case 4.

tunnels under the influence of dominant flow is of vital importance to the prevention and control loess tunnel lining diseases. The authors simulate the possible joint seepage field by means of theoretical studies and numerical simulations and perform simulated calculations and analyses of tunnel forces under the influence of joint seepage, with a view to providing guidance and insight for the design and construction events of shallow buried loess tunnels affected by joints seepage.

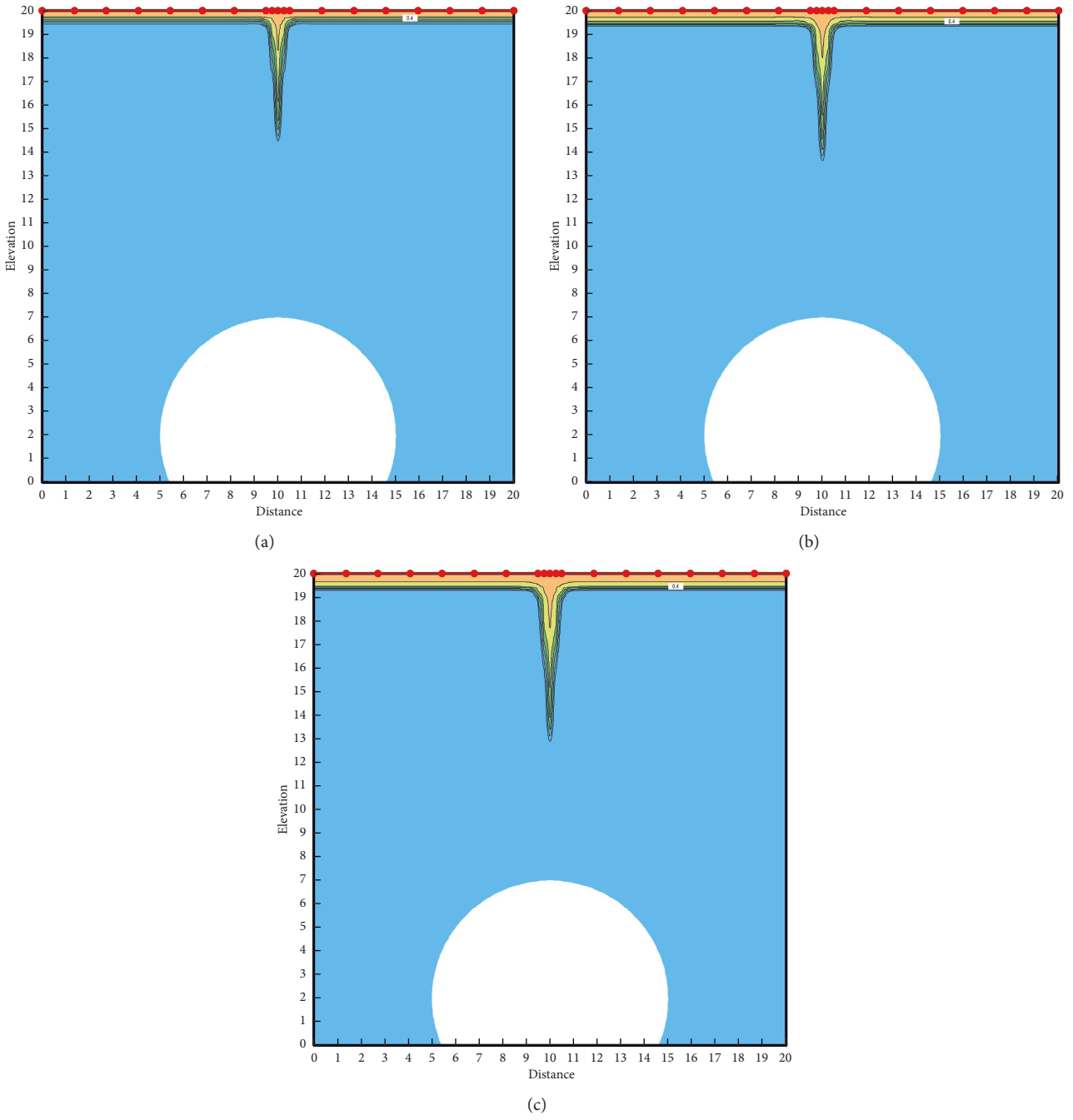

Figure 3: Case 1 3rd, 4th, and 5th hour seepage fields. (a) 3rd hour seepage field. (b) 4th hour seepage field. (c) 5th hour seepage field.

2. Seepage Numerical Simulation

2.1. Numerical Simulation. In this section, numerical simulations of seepage are performed for the established model of loess containing joints using the numerical simulation software GeoStudio. Figure 1 shows the seepage numerical calculation model and grid size. The longitudinal calculation range is 20 m, the vertical calculation ranges of both lateral sides are 20 m including 13 m buried depth. A circular impermeable layer was set at the bottom to simulate the tunnel lining, impermeable boundaries were set at the sides and bottom, and a 0.02 m pressure head was set at the top to simulate surface water accumulation. The saturated permeability coefficient of the loess is set to $5e-6$ m/s with an initial moisture content of 12%. The joints are located at the top and left sides of the impermeable layer. The length of the vault joints is 13 m, the left side joints are 20 m, and the size of the joints unit is $25\,\text{cm} \times 2.5\,\text{cm}$. The equivalent permeability coefficients of the joints are 2×10^{-3} m/s and 5×10^{-3} m/s, and four cases of 1, 2, and 3 joints directly above the impermeable layer and 1 joint above the left of the impermeable layer are set. The working conditions are shown in Table 1.

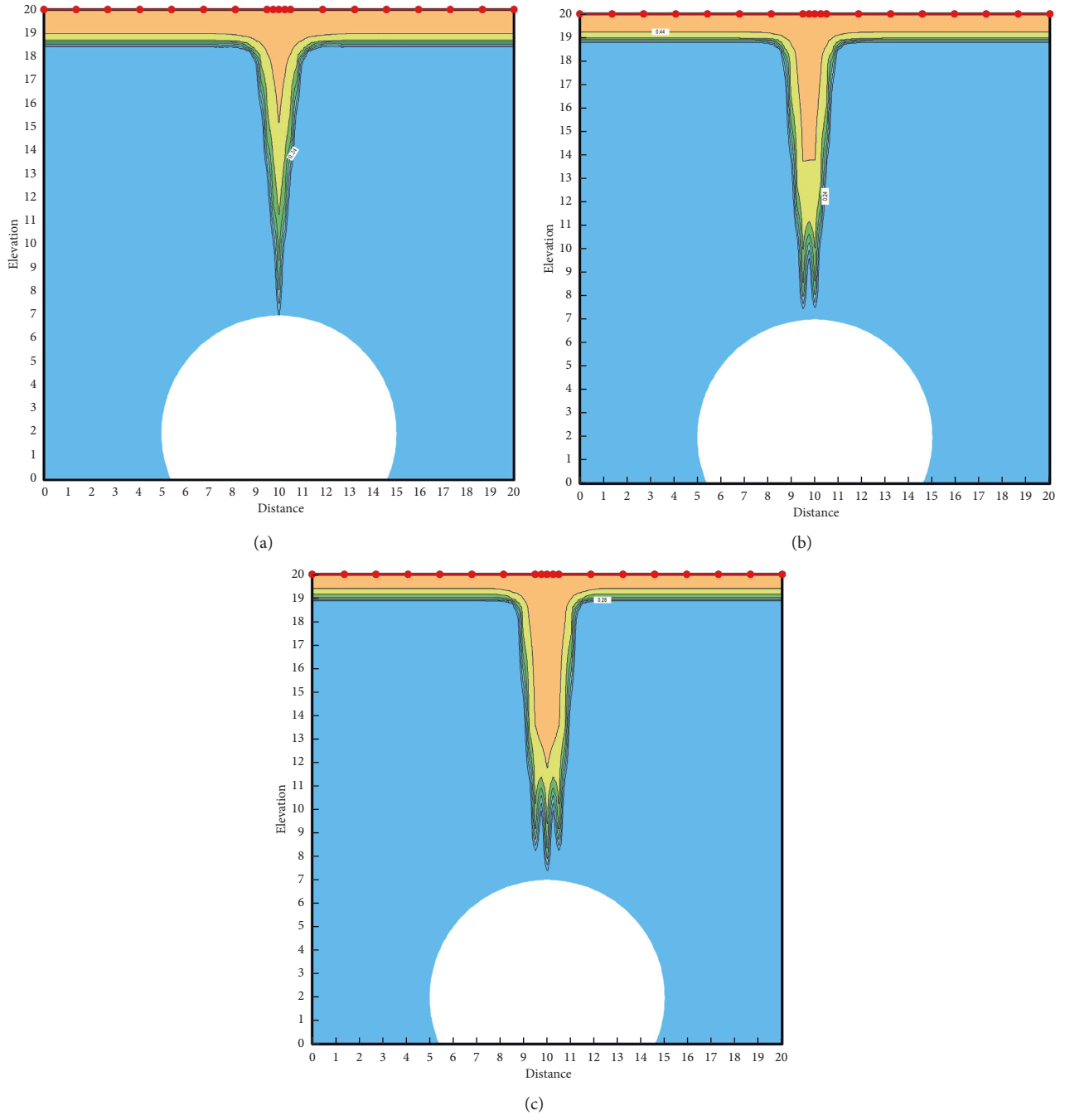

Figure 4: Seepage field of 1 hour before the wetting front touches the impermeable layer in Case 1, Case 2, and Case 3. (a) Case 1. (b) Case 2. (c) Case 3.

2.2. Results of Numerical Investigation. The 24% wetting front depths of Case 1, Case 2, Case 3, and Case 4 after the surface water started to infiltrate are shown in Figure 2. It can be seen that Case 1, Case 2, and Case 3 are three cases with the same nodal permeability coefficient, and their wetting fronts contact the impermeable layer after 11, 13, and 18 hours of the start of infiltration, respectively. The depth of the wetting front is relatively close within the first 3 hours of the beginning of infiltration, indicating that the number of nodules at the beginning of infiltration has less influence on the advance rate of the wetting front. After 3 hours, the infiltration rate of 1 and 2 joints began to slow down and the advancing depth curve of the wetting front leveled off, while the infiltration rate of 3 joints remained basically the same and the advancing depth curve of the wetting front kept increasing linearly. Six hours after the start of infiltration, the advance of the wetting front in Case 1 slowed down further, while the advance of the wetting front in Case 2 did not decrease significantly.

Figure 3 shows the seepage field of Case 1 at the 3rd, 4th, and 5th hours after the start of infiltration. From the figure, it can be seen that, from the 3rd hour onwards, the region of

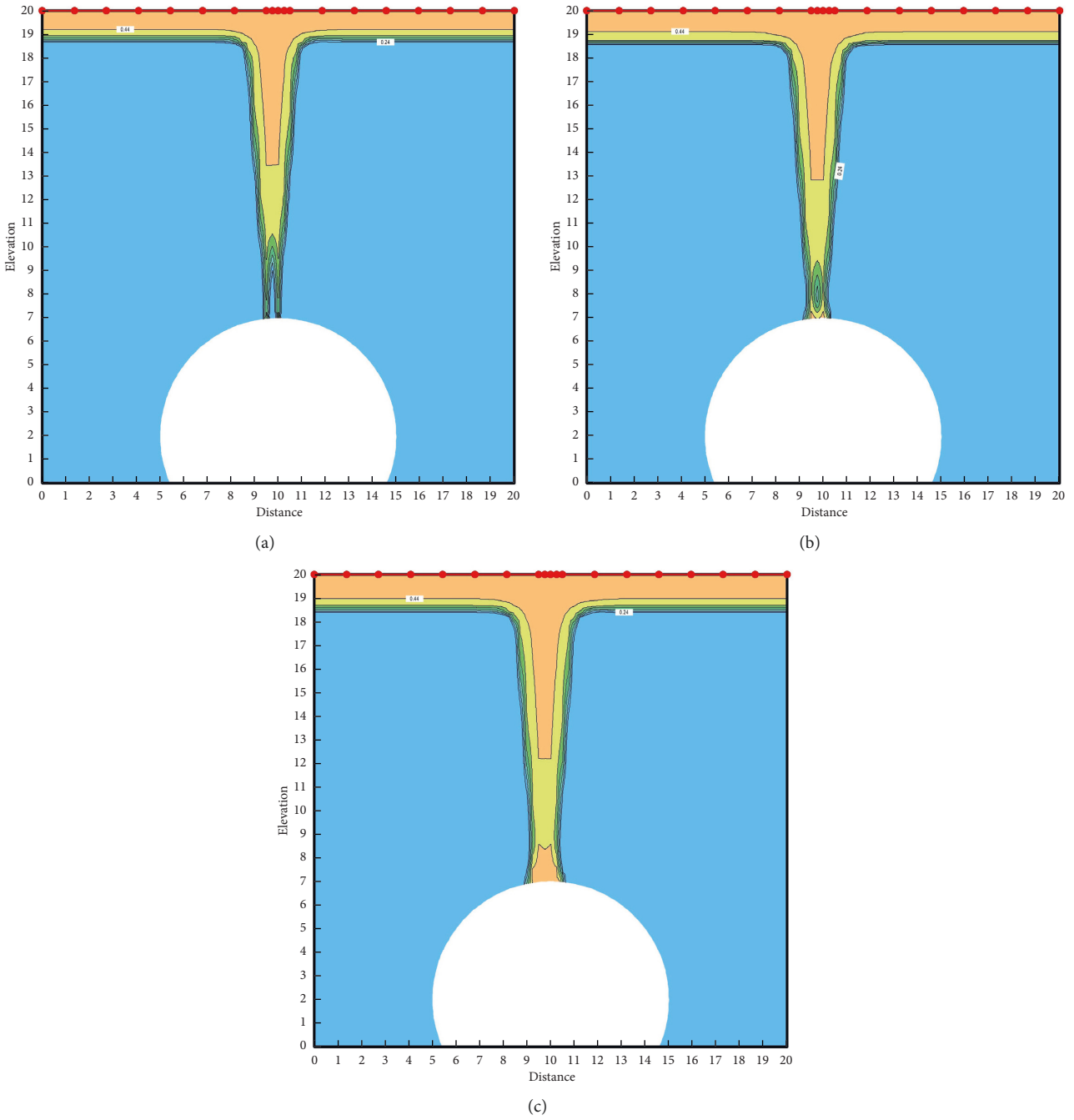

Figure 5: Seepage field after the 0th, 2nd, and 4th hours of contacting the impermeable layer by the wetting front in Case 2. (a) Hour 0 seepage field. (b) 2nd hour seepage field. (c) 4th hour seepage field.

40% water content starts to develop to both sides with the joints as the center, and the increase in lateral infiltration is precisely the reason for the further decrease in the forward speed of the wetting front of Case 1. This phenomenon can also be observed in Case 2, where both Case 1 and Case 2 have a phase where the saturation zone expands, and the advancing speed of the wetting front decreases, after which the advancing speed of the wetting front is further stabilized. However, this phase is shorter in Case 2. Case 2 and Case 3 have greater infiltration per unit time due to the increase in the number of nodules, bringing a wider and deeper saturation zone while also allowing a greater depth of advancement of the 24% moisture content wetting front.

Figure 4 shows the seepage fields of the wetted fronts before contacting the impermeable layer for 1 hour in Case 1, Case 2, and Case 3. As can be seen in Figure 4, the depth of the saturated zone under the working condition of 1 joint is less than half of the depth of the wetting front at 24% water content, and the saturation zone is conical in shape with a very narrow width. The depth of the saturation zone is greatly

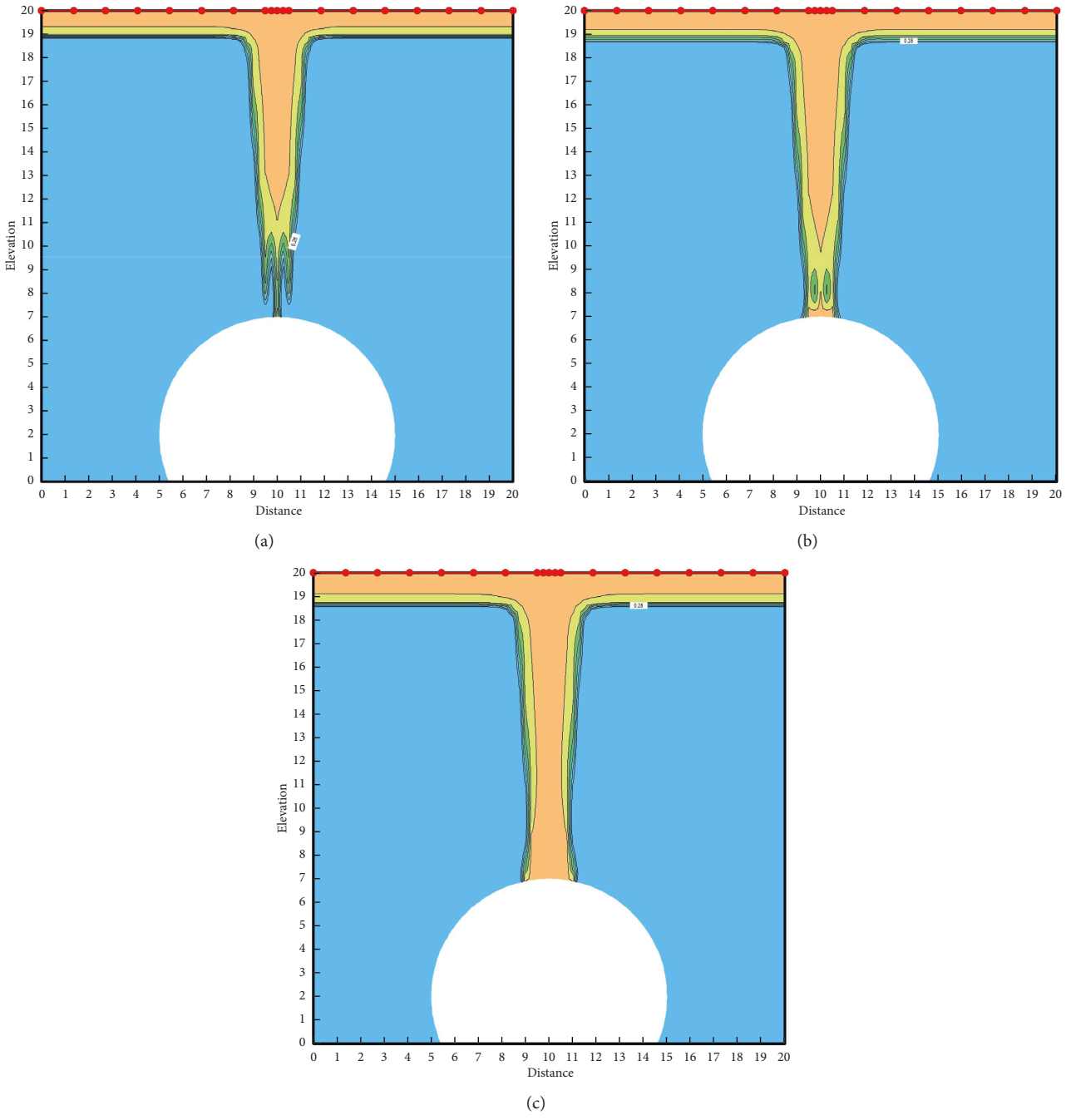

Figure 6: Seepage field after the 0th, 2nd, and 4th hours of contacting the impermeable layer by the wetting front in Case 3. (a) Hour 0 seepage field. (b) 2nd hour seepage field. (c) 4th hour seepage field.

increased for the cases of 2 joints and 3 joints. The depth of the saturation zone reaches half of the wetting front of 24% water content in Case 2 and 2/3 of the wetting front of 24% water content in Case 3. The width of the saturation zone also increases with the increase of the number of joints. It can be assumed that the increase in the number of joints contributes to the increase in the depth and width of the saturated zone, and the increase in the depth and width of the saturated zone also accelerates the advance of the wetting front.

Figures 5 and 6 show the seepage fields after the 0th, 2nd, and 4th hours of contacting the impermeable layer for the wetting front in working conditions 2 and 3, respectively. It can be seen that the number of joints has a significant effect on the extent of the saturation zone after the wetting front contacts the impermeable layer. Compared with that in Case 3, the saturation zone in Case 2 appears slower and smaller in width, and Case 2 does not have the rapid penetration of the saturation zone in Case 3. At the same time, both working conditions showed a parallel distribution of equal water content lines after the wetting front contacted the impermeable layer, forming a rectangular wetting zone in the soil.

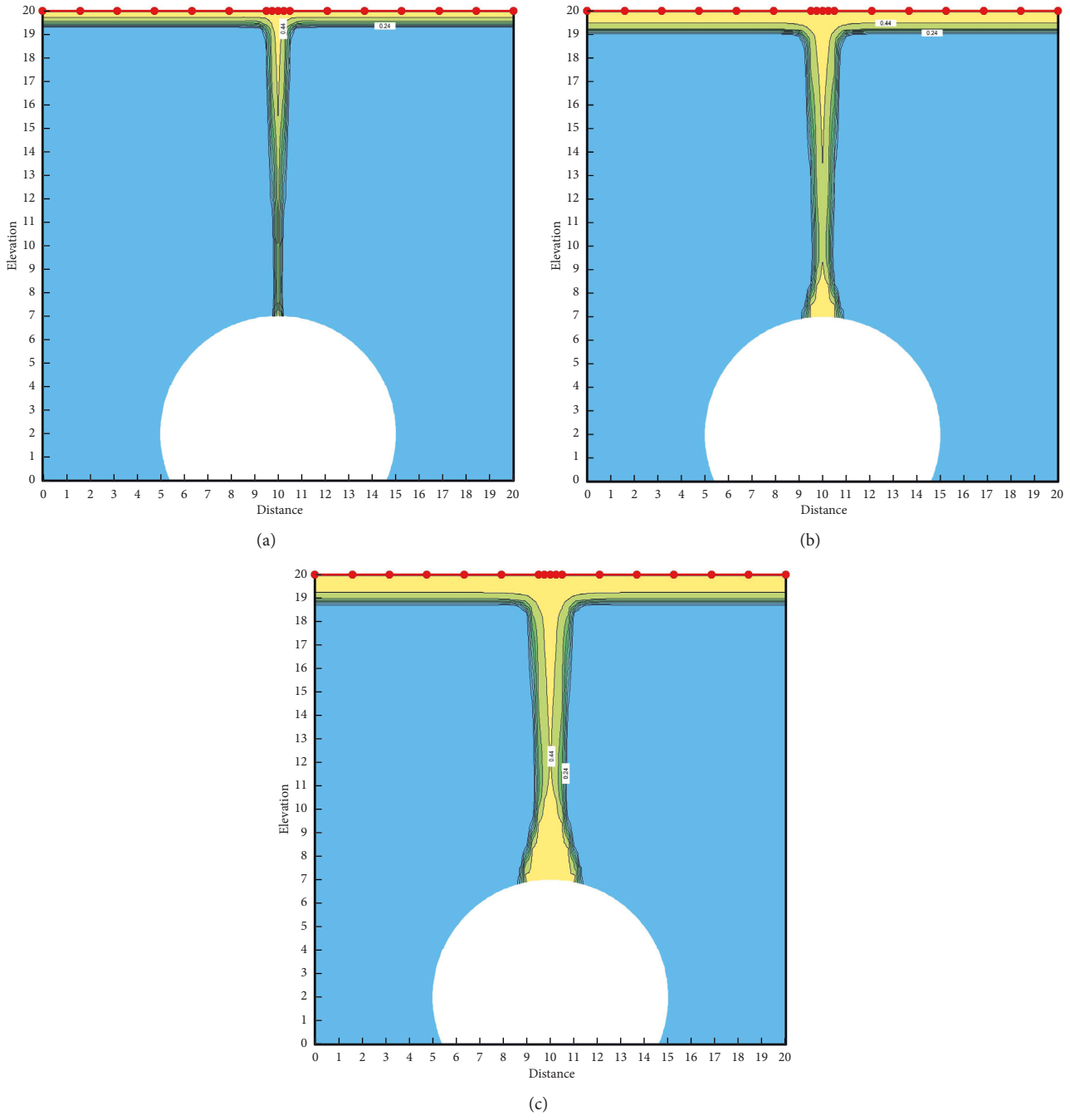

Figure 7: Seepage field after 4, 8, and 12 hours of infiltration in Case 4. (a) Seepage field after 4 hours. (b) Seepage field after 8 hours. (c) Seepage field after 12 hours.

Figure 7 shows the seepage field after 4, 8, and 12 hours of infiltration at the beginning of working Case 4. It can be seen that, in the surface water infiltration process species, the infiltration coefficient of 5×10^{-3} m/s joints will cause surface water to fill the ground. The infiltration of water between 4 and 8 hours is mainly in the impermeable layer above the siltation, so that the soil above the impermeable layer quickly reaches saturation. The saturation area on the impermeable layer reaches the maximum width, and the width gradually decreases upward, and the central part of the soil is in a state of near saturation but is not saturated. The saturated area is gradually connected upwards and downwards within 8 to 12 hours, but the width of the saturated area in the middle is very small, which fully indicates that the surface water infiltration is irrigation type, and the lateral infiltration coefficient is much smaller than the longitudinal infiltration coefficient. The infiltrated water mainly accumulates at the bottom, which causes the formation of a very wide saturated area in the upper part of the impermeable layer.

Figure 8 shows the seepage field at the beginning of infiltration after 6, 9, and 12 hours of working Case 5. It can

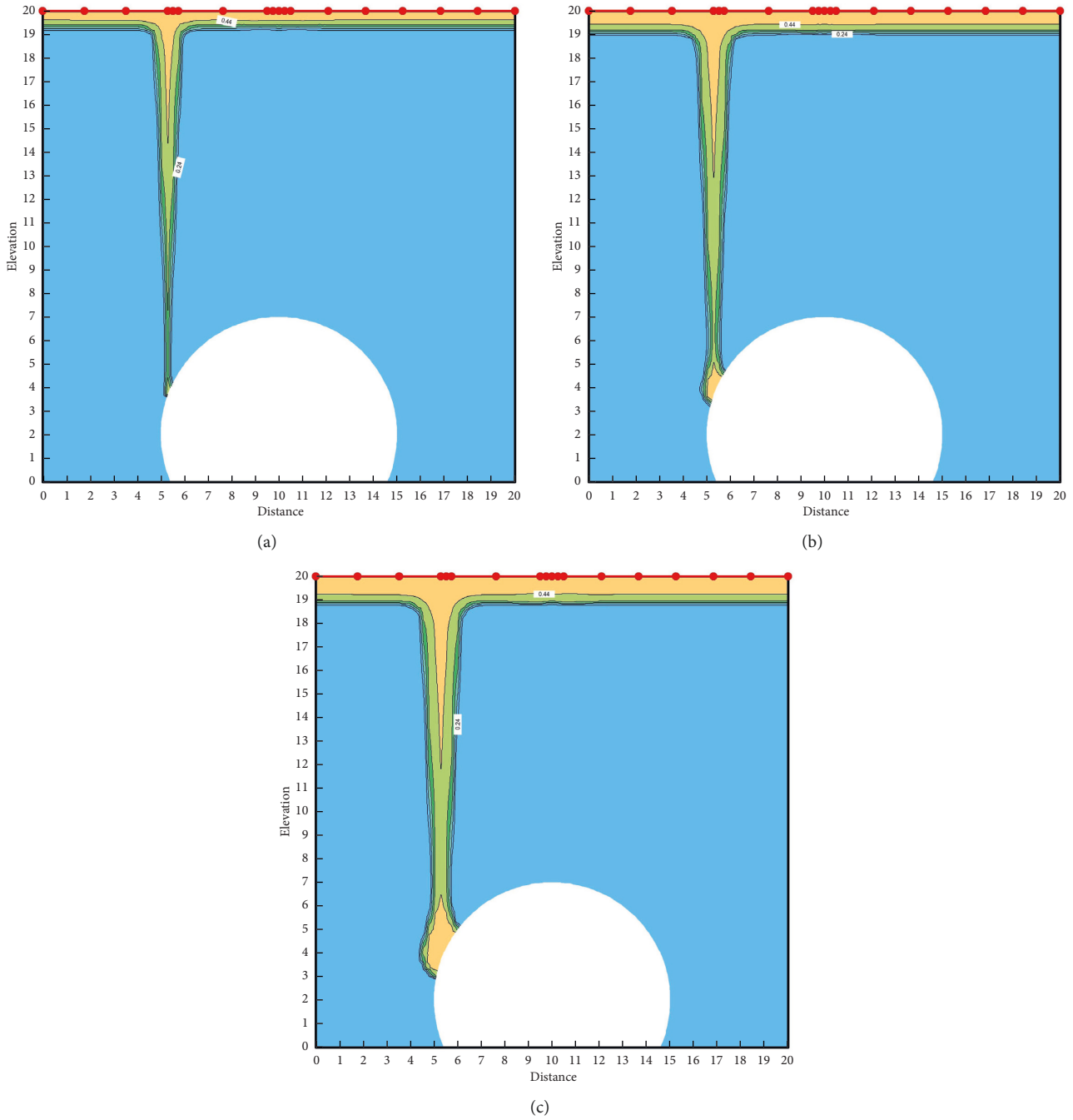

Figure 8: Seepage field after 6, 9, and 12 hours of infiltration in Case 5. (a) Seepage field after 6 hours. (b) Seepage field after 9 hours. (c) Seepage field after 12 hours.

be seen from the figure that seepage fields of working condition 5 and working condition 4 are similar; both of them have a high saturation area of 40% water content after the wetting front touches the impermeable layer for 1 hour. Then the infiltrated water mainly accumulates at the lowest end of the joints and on the impermeable layer, and a relatively large saturation area will be formed on the impermeable layer. Unlike working condition 4, in working condition 5, the infiltrating water flows below the impermeable layer under the action of gravity, and it moves from the arch shoulder and arch side to the foot of the arch, forming a saturated area with a small top and a large bottom.

2.3. Numerical Simulation Analysis considering Liner Drainage System. Road tunnel is equipped with drainage system which contains circular, longitudinal, as well as horizontal drainage pipes behind the lining. The drainage effect of the tunnel lining should be taken into account when performing seepage simulations related to perimeter rock

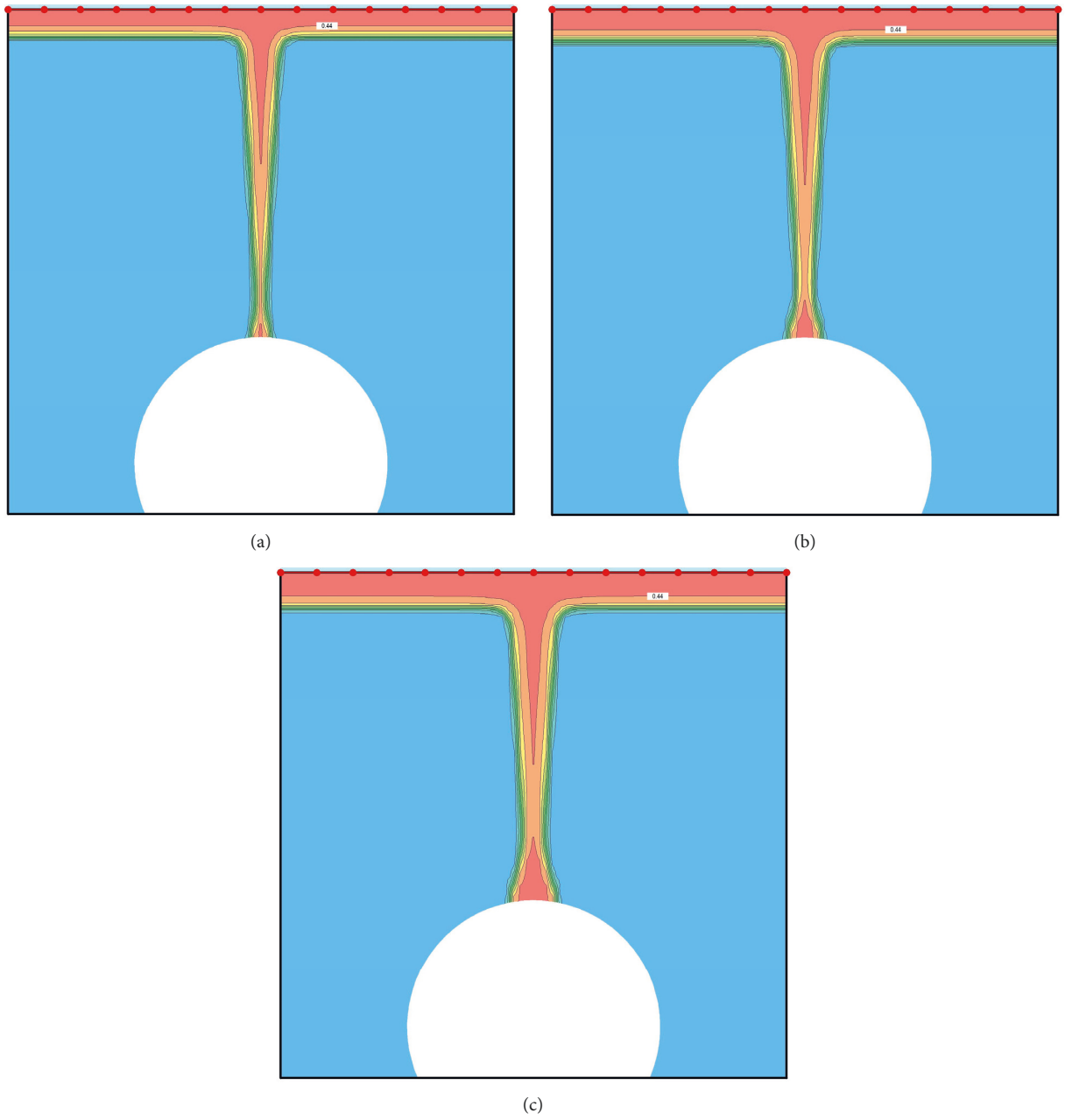

Figure 9: Seepage field after 8, 10, and 12 hours of infiltration in Case 1, lining without drainage system. (a) Seepage field after 8 hours. (b) Seepage field after 10 hours. (c) Seepage field after 12 hours.

seepage. To simplify the calculation process and by reviewing the relevant literature, the tunnel lining is simplified to a permeable surface in the simulations in this chapter to simulate the perimeter rock seepage under effective working conditions of the lining drainage system.

Figures 9 and 10 show the seepage flow field of Case 1 for the liner without and with drainage system, respectively. It can be seen that the surrounding rock at the edge of the tunnel lining is saturated at the 8th hour, regardless of whether the tunnel lining has drainage or not. However, with the increase of seepage time, the seepage fields of the two different working conditions appear to be significantly different. When the tunnel lining does not have drainage capacity, the saturated area at the top of the tunnel will expand rapidly, creating a large saturated area at the top of the tunnel in just 2 hours. When the tunnel lining had drainage capacity, the saturated zone of the surrounding rock at the top of the tunnel showed no significant growth in width or height after the 8th hour formation. It can be seen that the most important role of the existence of the lining drainage system is to effectively prevent the problem of water accumulation in the surrounding rock of the tunnel. When the liner drainage system is present, a near-rectangular seepage field

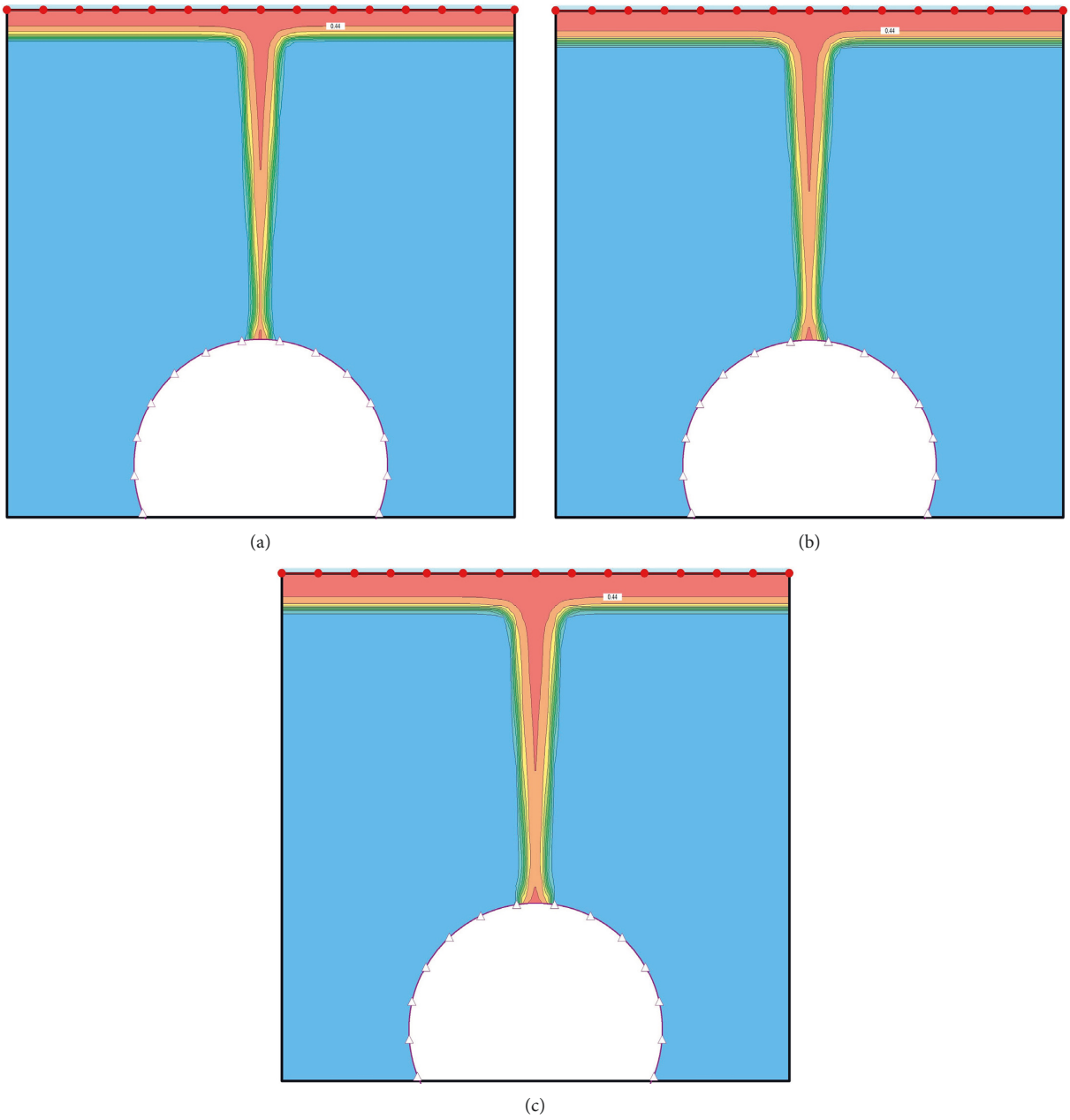

Figure 10: Seepage field after 8, 10, and 12 hours of infiltration in Case 1, lining with drainage system. (a) Seepage field after 8 hours. (b) Seepage field after 10 hours. (c) Seepage field after 12 hours.

centered at the joint position is formed in the surrounding rock.

3. Influence of Joint Seepage on the Mechanical Behavior of Existing Tunnels

3.1. Analytical Model and Calculation Parameters. According to the viewpoint of elastic mechanics, the model is simplified to a plane strain problem for study, and a two-dimensional calculation model is established. The model size is 50 m × 35 m, the width of the tunnel is 10 m, the height is 7 m, and the model size is set to five times of the tunnel size to ensure the accuracy of the calculation. Horizontal and vertical displacement constraints are set at the bottom of the model, horizontal displacement constraints are set on both sides of the model, the top is a free surface, and the computational model and mesh are shown in Figure 11.

In this model, the stress field of the loess stratum in its natural state is calculated according to the material properties in Table 2, and the ideal elastoplastic principal structure model with the Mohr–Coulomb strength criterion is used to calculate the tunnel. The tunnel is excavated by killing the unit, and the C20 concrete lining with a thickness of 25 cm and anchor rod support are applied after 30 steps of calculation to simulate the construction method of applying the lining immediately after excavation. The concrete lining

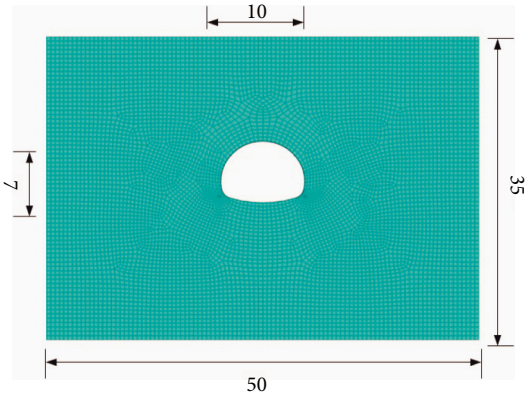

Figure 11: Numerical calculation model of tunnel.

Table 2: Material parameters.

Loess	Gravity (kN/m^3)	Cohesive force (kPa)	φ (ϕ/°)	Elastic modulus (MPa)	Poisson's ratio (μ)
Natural water content	15.2	36	26	22.62	0.32
Water immersion	17.7	9	18	2.26	0.32

Table 3: Material parameters.

Material category	Gravity (kN/m^3)	Elastic modulus (GPa)	Poisson's ratio (μ)	K (GPa)	G (GPa)
Lining	25	25.3	0.2	17.5	13.1

Table 4: Material parameters.

Material category	Gravity (kN/m^3)	Yield strength (MPa)	E (GPa)	Diameter (mm)	Poisson's ratio (μ)	Length (m)
Bolts	78.5	500	200	42	0.2	2.5

is simulated using the shell unit (the concrete lining is simulated by shell unit (shell), and the anchor rod is simulated by anchor cable unit (cable)). Material properties of the surrounding rock are based on existing literature [24, 25]. The properties of each material are shown in Tables 3 and 4.

Different joints locations and permeability coefficients will produce saturated areas with different locations and widths. Five working conditions are set up as shown in Table 5 and Figure 12 according to the different joints locations and permeability strengths.

Table 5: Working condition setting.

Case	Infiltration depth (m)	Joint distribution	Infiltration width (m)
1	2	—	-
2	2	Arch vault	3
3	2	Arch vault	5
4	2	Spandrel	3
5	2	Arch foot	3

3.2. Surface Settlement Analysis. The surface settlement curves of the five working conditions after the rainfall-induced waterlogging of the surrounding rock are shown in Figure 13. It can be seen that the settlement curve after the immersion of the surrounding rock has a quadratic parabolic distribution, and there is a strong correlation between the surface settlement and the location of the surrounding rock immersion. In Case 1, there is only uniform infiltration, the settlement trough width is about 25 m, the settlement curve is symmetrical along the central axis of the tunnel, and the maximum settlement occurs directly above the tunnel vault with a settlement value of 7.49 mm. The settlement troughs of the other four conditions with nodal infiltration are all enlarged, with the settlement trough of Case 2 exceeding 45 m.

The settlement curves of Case 2 and Case 3, which are symmetrical in the infiltration and wetting zone of the joint, are symmetrical along the central axis of the tunnel as in Case 1, and the maximum settlement also occurs directly above the vault, with settlement values of 14 mm and 21.8 mm. We introduce the concept of a settlement trough to illustrate the effect of the presence of the tunnel on the

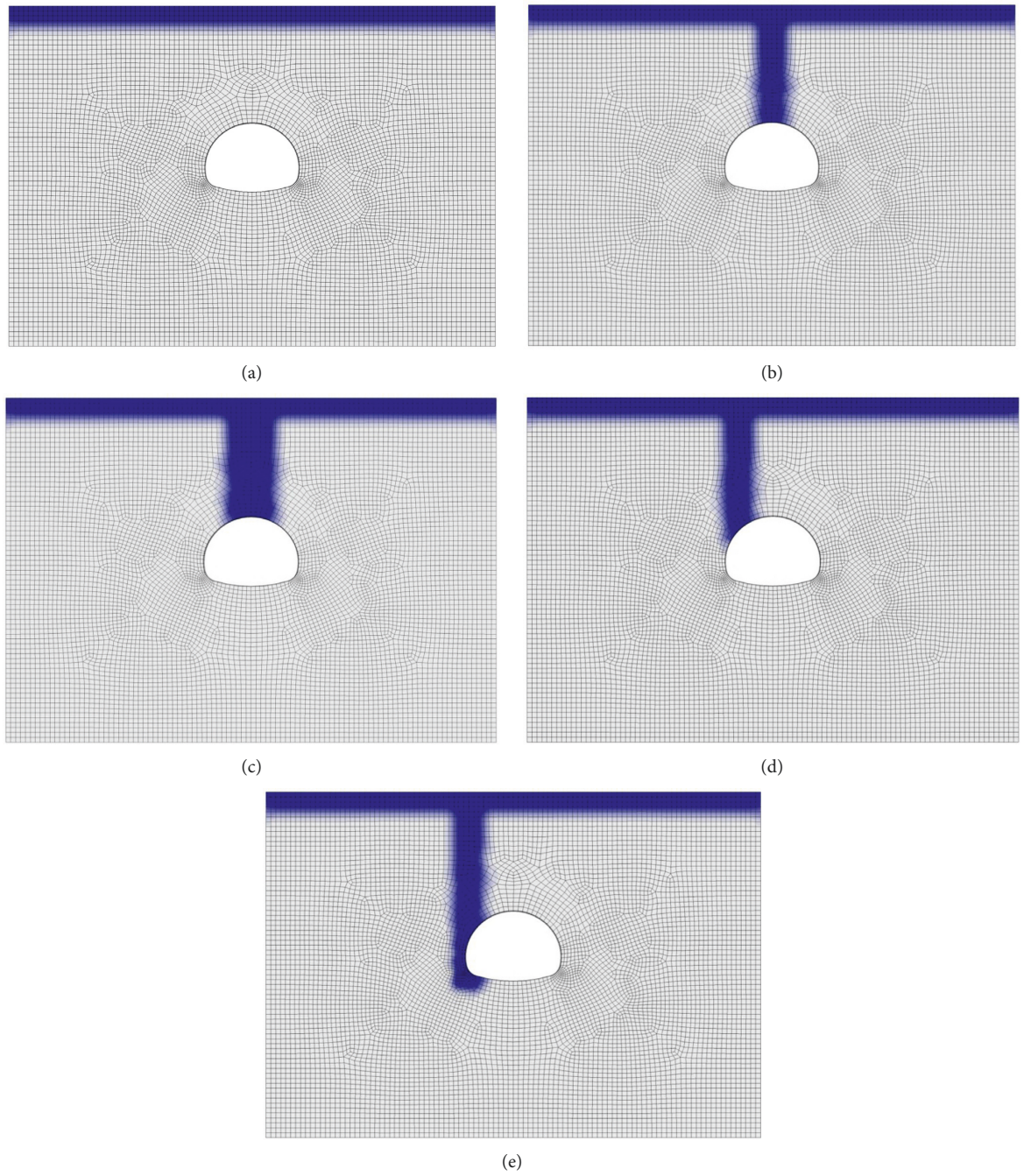

Figure 12: Working condition setting. (a) Case 1. (b) Case 2. (c) Case 3. (d) Case 4. (e) Case 5.

settlement of the surrounding rock. We approximated the settlement trough curve as a quadratic parabola, taking the 2 m uniformly infiltrated loess settlement plane as the x-axis, and the range of the settlement trough is determined according to the two intersection points of the parabola and the x-axis. Among the five working conditions, the surface settlement value of working condition 3 is the largest, and the settlement trough of Case 3 is significantly larger than those of Case 1 and Case 2, reaching about 50 meters. This indicates that the increase of the submerged water range significantly affects the surface settlement range and depth.

The width of the immersed area is the same for Case 4, Case 5, and Case 2, but the maximum settlement has increased, and the settlement trough is wider. It can be seen that the settlement value of Case 5 is further expanded, the settlement trough is significantly wider and deeper, and the settlement above the vault is larger, indicating that the influence of the arch foot dip on the surface settlement is more significant.

3.3. Surrounding Rock Displacement Analysis. The monitoring points of rock displacement data are shown in

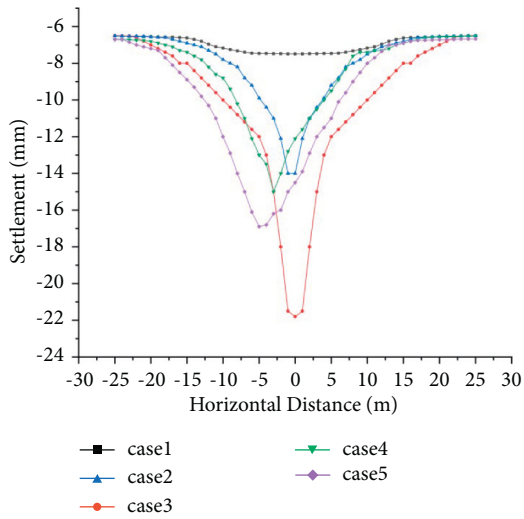

Figure 13: Surface settlement in each working condition.

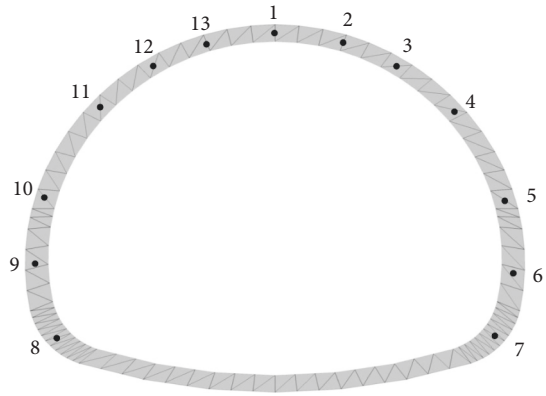

Figure 14: Surrounding rock displacement monitoring point.

Figure 14, and a total of 13 monitoring points including arch top, arch shoulder, arch foot, and arch waist are set.

Figure 15 shows the vertical displacements of each characteristic point after the waterlogging of the surrounding rock for the five working conditions.

It can be seen that a certain amount of settlement occurs at each characteristic point in Case 1, among which the settlement value of the vault is the largest, and the settlement of each part of the lining is symmetrically distributed with the central axis as the center. This symmetry also appears in Case 2 and Case 3.

In Case 2 and Case 3, where the arch is submerged in water, there is a significant increase in arch settlement, and the settlement curve has a secondary parabolic distribution with the central axis of the arch as the symmetry axis, and the tunnel shows a flattening trend.

The maximum settlement value of Case 2 is increased by about 83% compared with Case 1. With the increase of the dip range of the arch, the self-weight of the surrounding rock increases and the bearing capacity of the surrounding rock decreases. The vertical displacement of each characteristic point in Case 3 has increased, among which the settlement value of the arch top has increased the most, an increase that is 119% higher than that of Case 1.

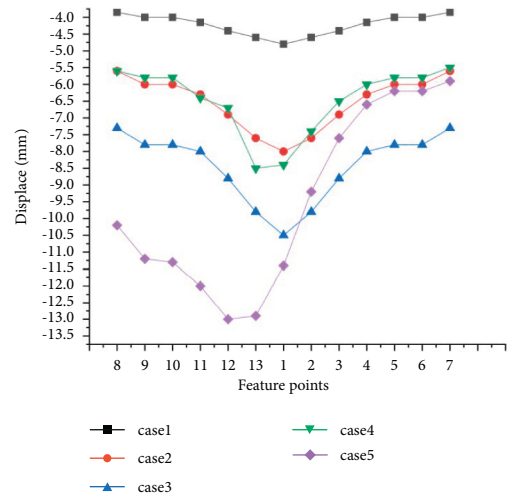

Figure 15: Settlement folding diagram of surrounding rock for each working condition.

The submerged areas of both Case 4 and Case 5 are located on the left side of the tunnel, with Case 4 being located above the vault and Case 5 on the left side and left foot of the tunnel. It can be seen that the overall settlement of Case 4 is similar to that of Case 2, except that the settlement curve of Case 4 is asymmetrically distributed, and the maximum settlement occurs at the left arch shoulder and at the top of the arch. Figure 16 shows the vertical rock displacement cloud of Case 5. It can be seen that the surrounding rock on the submerged side of the tunnel in Case 5 showed significant settlement.

Figures 17 and 18 show the horizontal displacement clouds of the surrounding rock for Case 4 and Case 5. It can be seen that water immersion on the left side of the tunnel causes the overall displacement of the tunnel to the right. In Case 4, the tunnel as a whole is compressed and flattened. The left side of the surrounding rock displaced to the left and the right side displaced to the right, with the right side having a greater displacement value. In working condition 5, due to the waterlogging of the arch foot, the soil arch effect of the tunnel surrounding rock is destroyed, and the bearing capacity is greatly reduced, and there is a tendency for the tunnel to be displaced to the right as a whole. In particular, the displacement of the right is significantly increased.

4. Impact of Joint Seepage on Tunnel Construction

4.1. Numerical Simulation Program. This section describes how the shallow buried loess tunnel is simulated for working Case 2, working Case 3, working Case 4, and working Case 5 using two construction methods: the three-step method and the Cross middle door method, that is, CRD.

The model and grouping of the three-step construction method are shown in Figure 19. The simulation procedure is as follows: first, the model is established, values are assigned to the surrounding rock, boundary conditions are applied, and the simulation of the wet zone is carried out after the

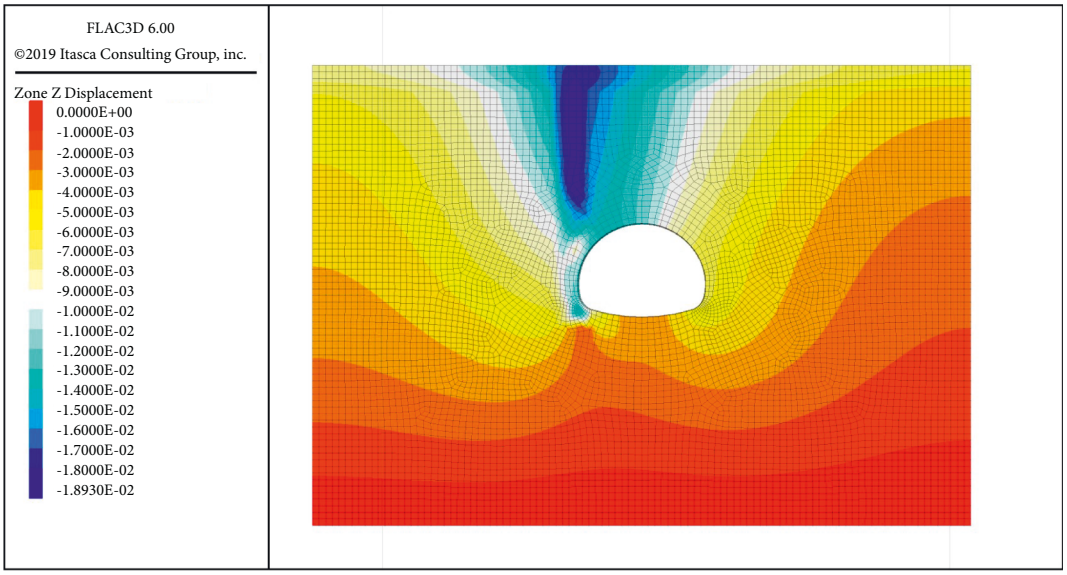

Figure 16: Case 5 vertical displacement cloud of surrounding rock.

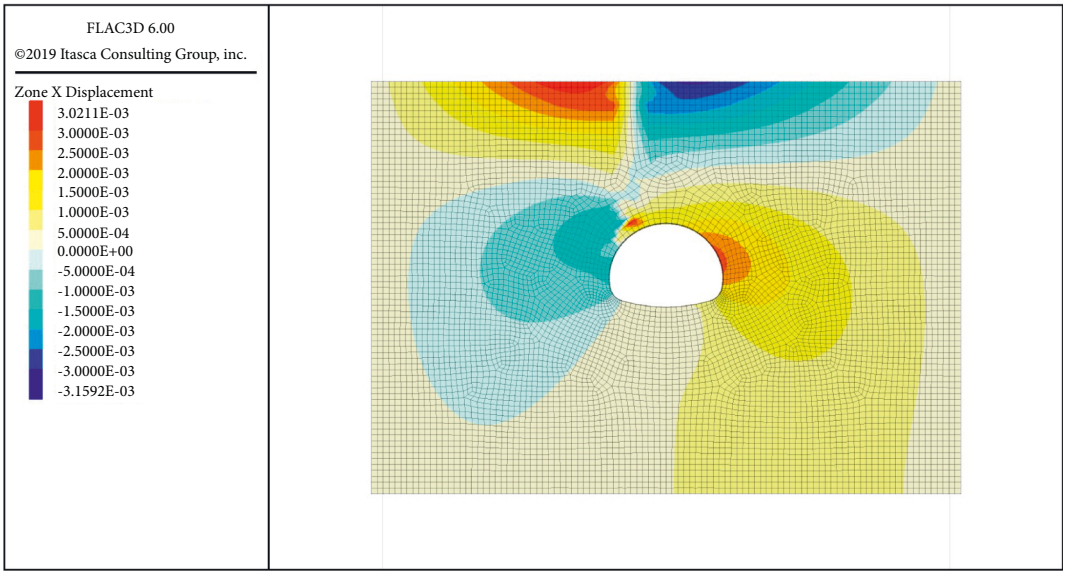

Figure 17: Case 4 horizontal displacement cloud of surrounding rock.

initial equilibrium. After calculating the stress in the wet zone, the displacement and velocity are zeroed to start the excavation, and the concrete lining and anchor support are applied according to the excavation of step A. The excavation of step B, the concrete lining, and anchor support are applied. Finally, the excavation of step C, the concrete lining, and anchor support are applied.

The model and grouping for the construction of the CRD method are shown in Figure 20. The simulation procedure is as follows. Firstly, the model is built, values are assigned to the surrounding rock, boundary conditions are imposed, and the wet zone after the initial equilibrium is simulated. After calculating the stress in the wet zone, the displacement and velocity are zeroed, and the excavation is started. According to the excavation of the upper left A step, the concrete lining and anchor support are applied. The upper right B step is excavated, and the concrete lining and anchor support are applied. The lower left C step is excavated, and the concrete lining and anchor support are applied. Finally, the lower right D step is excavated, and the concrete lining and anchor support are applied.

4.2. Surface Settlement Analysis. The tunnels have different flooding conditions, and the surface settlement is generated after the excavation was completed using different excavation methods. The surface settlement curves after the completion of the excavation by the three-step method and the CRD method are shown in Figures 21 and 22.

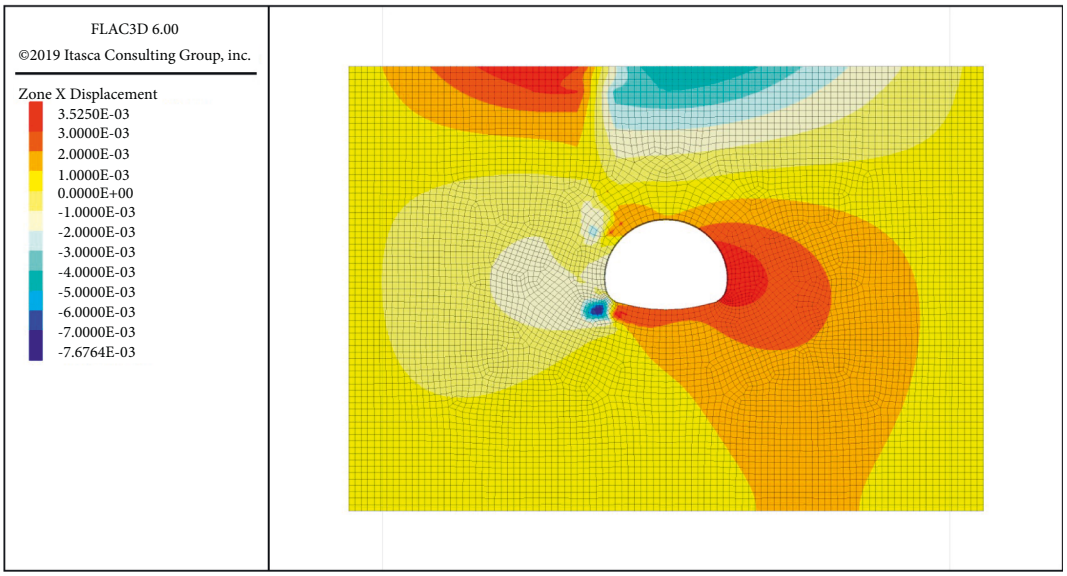

Figure 18: Case 5 horizontal displacement cloud of surrounding rock.

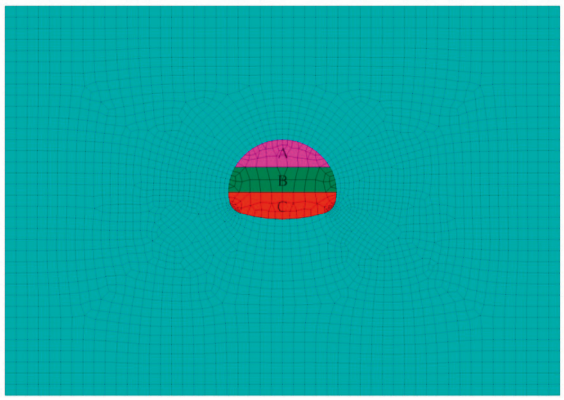

Figure 19: Numerical calculation model of three-step method construction.

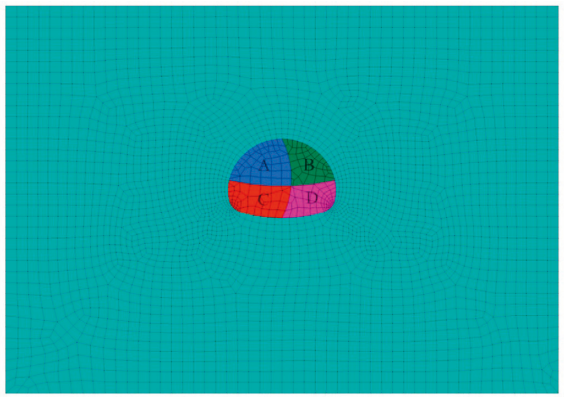

Figure 20: Numerical calculation model of CRD method construction.

It can be seen from Figure 19 that the surface soil showed a certain settlement trend after the completion of the construction of the three-stage method under each soaking condition, and, with the increase of the vault soaking area, the vault settlement in Case 3 increased slightly compared with that in Case 2, but the increase was small. Figure 23 shows the vertical ground stress cloud of Case 2, which shows that the vertical stress in the middle of the submerged area is increased, the soil arch effect is produced on both sides, and the soil in the middle is extruded and raised.

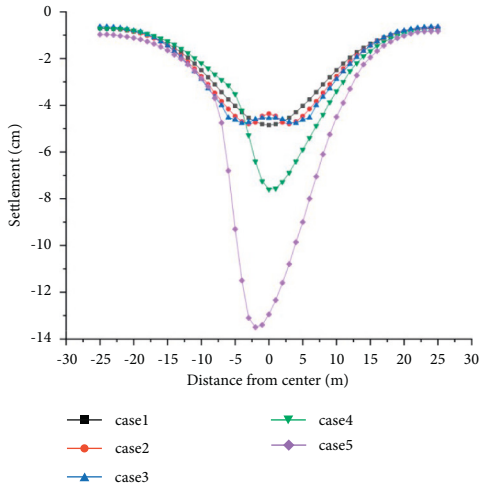

Figure 21: Surface displacement after the completion of the three-step method construction.

The width of the submerged area in Case 4 and Case 5 is the same as that in Case 2, but the surface settlement is much larger than that in Case 1, with the maximum settlement value in Case 4 increasing by 60% compared with that in Case 2 and the maximum settlement value in Case 5 increasing by 185% compared with that in Case 2. It can be seen that the surface settlement caused by the arch shoulder and the arch foot dip condition is much larger than that of the arch top dip condition. Figure 24 shows the vertical ground stress cloud diagram of Case 5. It can be seen from

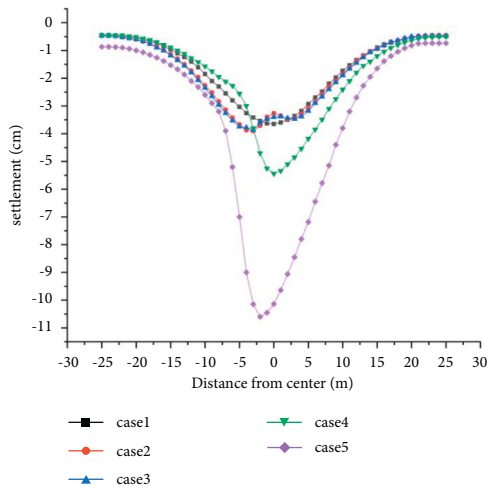

Figure 22: Surface displacement after the completion of the CRD method construction.

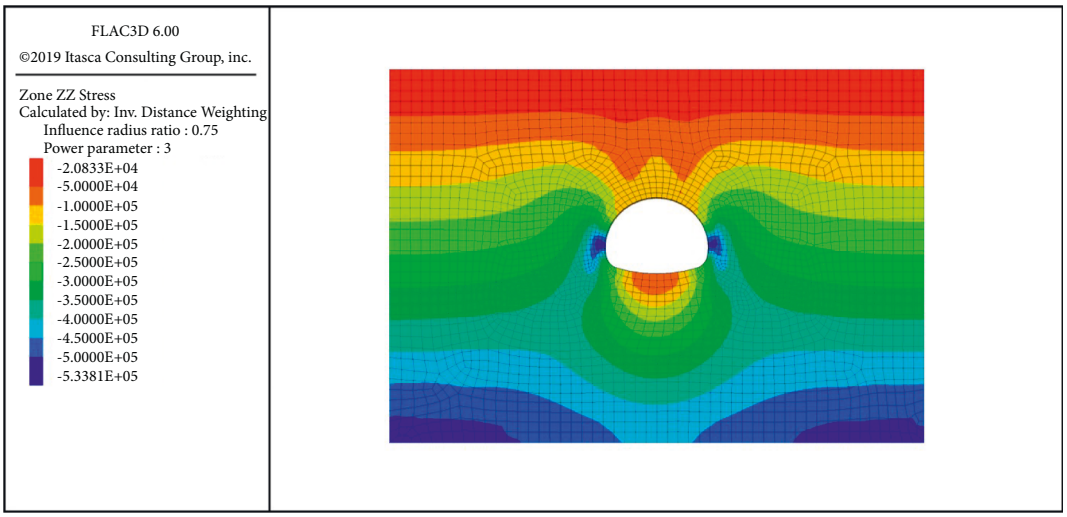

Figure 23: The vertical ground stress cloud of Case 2.

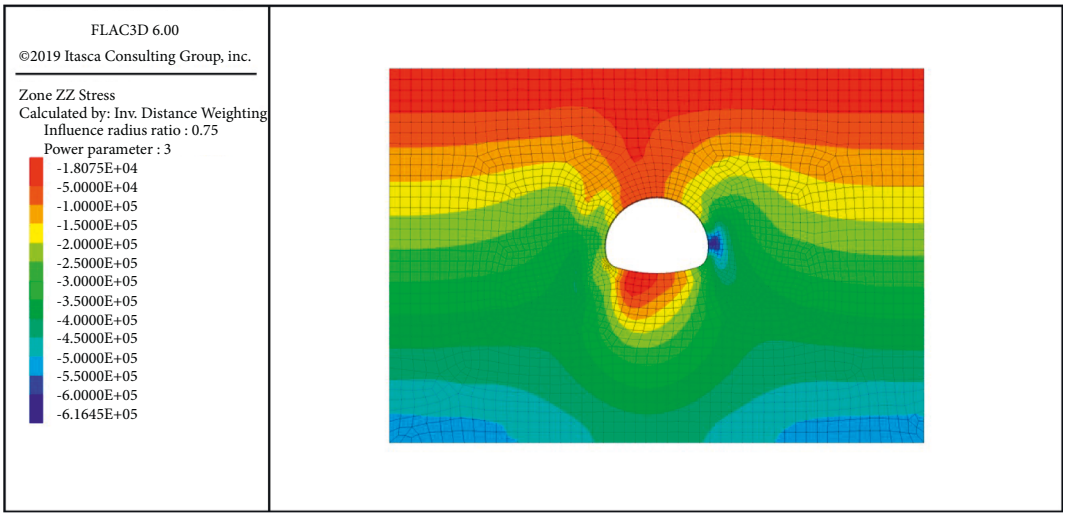

Figure 24: The vertical ground stress cloud of Case 5.

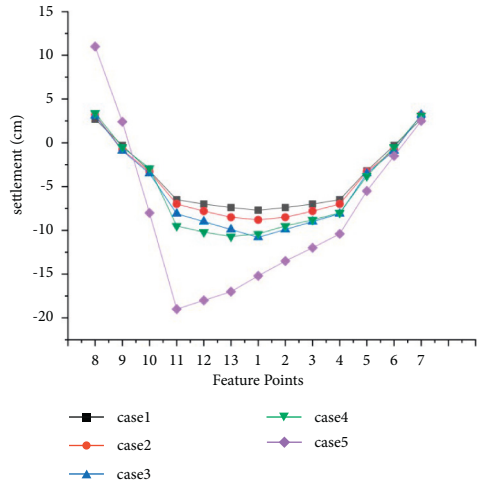

Figure 25: Vertical displacement of the surrounding rock after the completion of the three-step method.

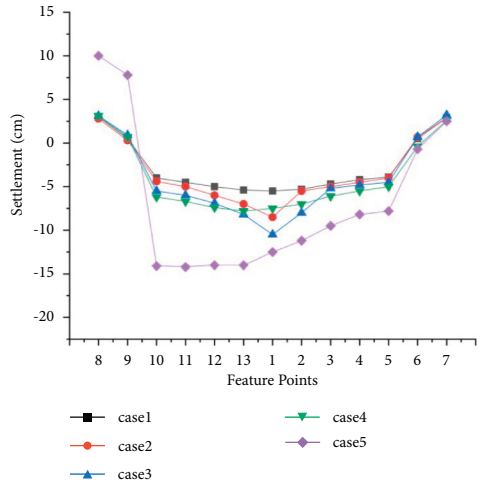

Figure 26: Vertical displacement of the surrounding rock after the completion of the CRD method.

Table 6: Vertical displacement of each working condition after excavation completion (cm).

Feature points	Case 1		Case 2		Case 3		Case 4		Case 5	
	Three-step	CRD	Three-step	CRD	Three-step	CRD	Three-step	CRD	Three-step	CRD
1	−7.7	−5.5	−8.8	−8.5	−10.8	−10.5	−10.4	−7.5	−15.2	−12.5
2	−7.4	−5.3	−8.5	−5.5	−9.9	−8	−9.5	−7	−13.5	−11.2
3	−7	−4.7	−7.8	−5	−9	−5.2	−8.8	−6.1	−12	−9.5
4	−6.5	−4.2	−7	−4.5	−8.1	−4.8	−8	−5.5	−10.4	−8.2
5	−3.2	−3.9	−3.3	−4	−3.5	−4.5	−3.8	−5	−5.5	−7.8
6	−0.3	0.5	−0.8	0.7	−0.9	0.7	−0.5	−0.4	−1.5	−0.7
7	2.7	2.9	3.2	2.9	3.2	3.2	3.1	2.6	2.5	2.5
8	2.7	3	3.2	2.8	3.1	3.1	3.4	3.1	11	10
9	−0.3	0.5	−0.8	0.3	−0.9	0.9	−0.5	0.7	2.4	7.8
10	−3.2	−4	−3.3	−4.4	−3.5	−5.5	−2.9	−6.2	−8	−14.1
11	−6.5	−4.5	−7	−5	−8.1	−6	−9.5	−6.7	−19	−14.2
12	−7	−4.9	−7.8	−6	−9	−6.9	−10.2	−7.4	−18	−14
13	−7.4	−5.3	−8.5	−7	−9.9	−8.2	−10.7	−7.8	−17	−14

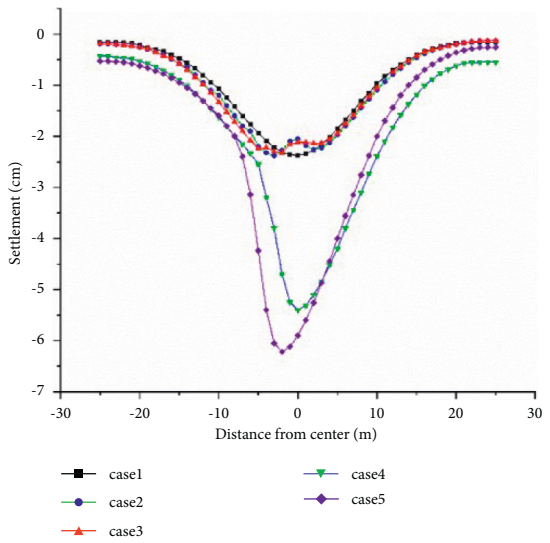

Figure 27: Surface displacement after the completion of the A-C-B-D sequence construction.

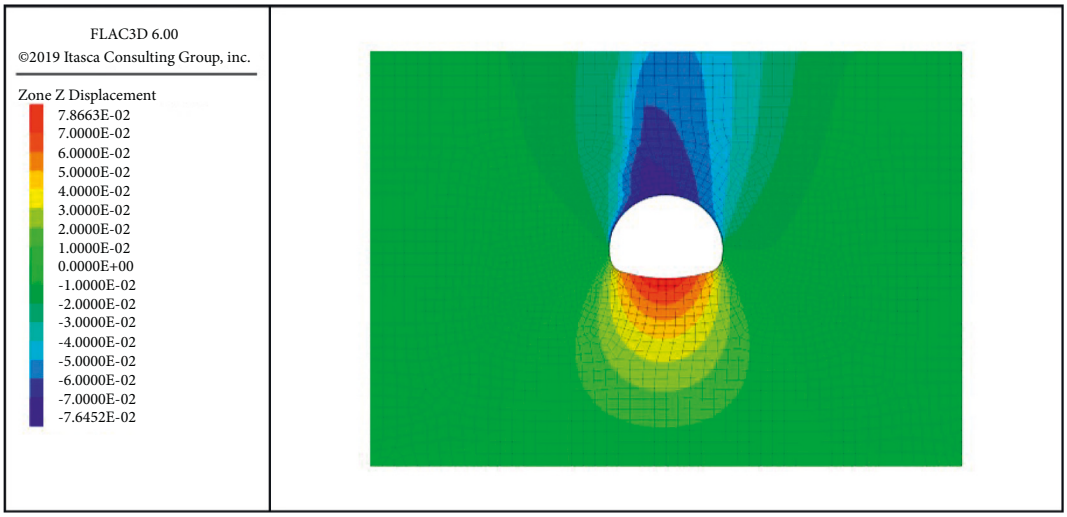

(a)

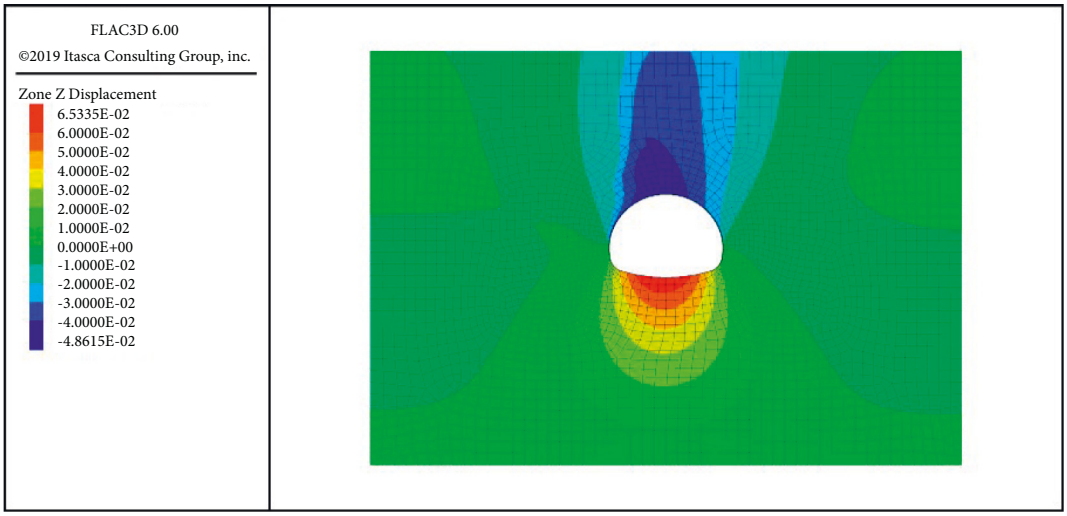

(b)

Figure 28: Case 4 vertical displacement cloud of surrounding rock. (a) A-B-C-D sequence. (b) A-C-B-D sequence.

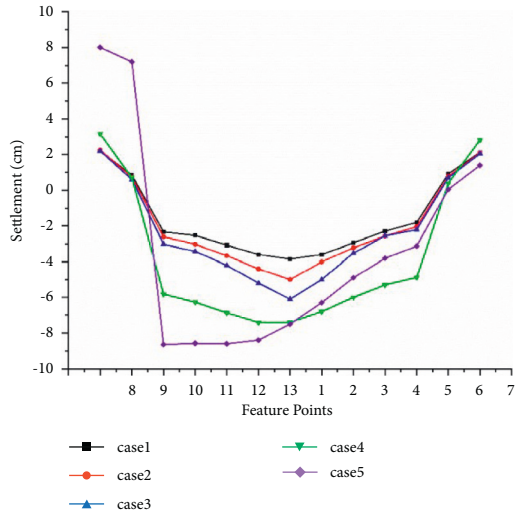

Figure 29: Vertical displacement of the surrounding rock after the completion of the A-C-B-D sequence construction.

Table 7: Vertical displacement of each working condition after excavation completion (cm).

Feature points	Case 1		Case 2		Case 3		Case 4		Case 5	
	A-B-C-D	A-C-B-D	A-B-C-D	A-C-B-D	A-B-C-D	A-C-B-D	A-B-C-D	A-C-B-D	A-B-C-D	A-C-B-D
1	−5.5	−3.8	−8.5	−5	−10.5	−6.1	−7.5	−7.4	−12.5	−7.5
2	−5.3	−3.6	−5.5	−4	−8	−5	−7	−6.8	−11.2	−6.3
3	−4.7	−2.9	−5	−3.2	−5.2	−3.5	−6.1	−6	−9.5	−4.9
4	−4.2	−2.3	−4.5	−2.6	−4.8	−2.5	−5.5	−5.3	−8.2	−3.8
5	−3.9	−1.8	−4	−2	−4.5	−2.2	−5	−4.9	−7.8	−3.1
6	0.5	0.92	0.7	0.78	0.7	0.7	−0.4	0.4	−0.7	0.1
7	2.9	2.13	2.9	2.1	3.2	2.1	2.6	2.8	2.5	1.4
8	3	2.2	2.8	2.3	3.1	2.2	3.1	3.1	10	8
9	0.5	0.85	0.3	0.73	0.9	0.6	0.7	0.7	7.8	7.2
10	−4	−2.32	−4.4	−2.6	−5.5	−3	−6.2	−5.8	−14.1	−8.65
11	−4.5	−2.52	−5	−3	−6	−3.4	−6.7	−6.3	−14.2	−8.58
12	−4.9	−3.05	−6	−3.7	−6.9	−4.2	−7.4	−6.9	−14	−8.6
13	−5.3	−3.58	−7	−4.4	−8.2	−5.2	−7.8	−7.4	−14	−8.4

Figure 24 that the vertical ground stress of the left side surrounding rock is greatly reduced due to the water immersion of the left arch foot, and the soil arch effect of the left arch foot is obviously weakened, which greatly weakens the bearing capacity of the surrounding rock.

Comparing the surface settlement after the completion of the three-stage method, it can be found that the surface settlement value decreases significantly after the construction of the cross-centralized next-door method, and the maximum value of surface settlement in each working condition is reduced by about 20%. From Figure 19, it can be observed that the settlement curves of Case 2 and Case 3 show two minimum points because the second relatively large settlement of the water-soaked surrounding rock at the top of the arch occurs after excavation of the B-stage. In both Case 4 and Case 5, the maximum settlement value point is located on the left side of the tunnel under the influence of water infiltration in the left side of the surrounding rock.

4.3. Surrounding Rock Displacement Analysis. The vertical displacement of the tunnel excavated by the three-step method after completion of excavation is shown in Figure 25. It can be seen that the maximum vertical displacement of working condition 1, working condition 2, and working condition 3 always appears at the top of the arch, the vertical displacement of arch shoulder and arch waist decreases in order, the vertical displacement of arch foot appears to be upward, and the displacement of arch bottom is between 2 and 3 cm, which is not much different. The arch top dip width has a certain influence on the arch top settlement, and the arch top settlements for the arch top dip condition in Case 2 and Case 3 are increased by 1.1 cm and 3.1 cm compared with Case 1, which have increase of 15% and 40%.

The maximum settlement of the surrounding rock in Case 4 appears in measurement point 13 between the left arch shoulder and the top of the arch, and the maximum value is 21.5% higher than that in Case 2. It can be seen that, for the same conditions of dip width, the influence of arch shoulder dip on the settlement of the surrounding rock is greater than that of arch top dip. The maximum settlement value of the surrounding rock in Case 5 is greatly increased compared with other cases. The maximum settlement value

is located in the left arch waist and above the lining, and the settlement value reaches 19 cm. It can be seen that the arch footing water immersion is the most unfavorable for tunnel construction settlement control. The existence of the wet zone of the tunnel arch shoulder and arch foot makes the tunnel be in a state of partial pressure, resulting in asymmetric vertical displacement. At the same time, due to the decrease in the bearing capacity of the surrounding rock in the wet zone, the self-supporting capacity of the rock above the tunnel decreases, and the tunnel lining is subjected to more external loads, so there will be a phenomenon of the vertical displacement being greater than other working conditions.

Figure 26 shows the vertical displacement of the tunnel excavated by the CRD method, and Table 6 shows the settlement values of the surrounding rock after excavation by the two excavation methods. It can be seen that, compared with the three-stage excavation method, the settlement of the tunnel using the CRD method is reduced under all conditions, which indicates that the CRD method is more advantageous in controlling the settlement of the surrounding rock.

In Case 2 and Case 3, the difference in the settlement of the arch roof after the completion of construction using two different construction methods is not large, but the settlement values of the shoulder and waist of the arch on both sides are significantly reduced. In Case 2, the settlement of the right lining is reduced by 35%, and the settlement of the left lining is reduced by 20%. In Case 3, the settlement of the right lining is reduced by 40%, and the settlement of the left lining is reduced by 25%.

In Case 4, the maximum settlement value was reduced by 27% by using the CRD method, and the settlement of the left arch shoulder was well controlled. In Case 5, excavation with the CRD method can largely avoid the huge settlement of 20 cm or more on the left arch waist and arch foot, and the maximum settlement is 26% lower than that of the three-step method. At the same time, the use of CRD method can make the overall settlement of the tunnel more uniform, and there will be no local huge settlement.

4.4. Comparative Analysis of Different Excavation Sequences of the Cross-Central Tunnel Method. This section describes the effect of using different excavation sequences on the forces and displacements in shallow buried loess tunnels during the construction of the cross-central tunnel method.

In the second paragraph of Section 4.1, the excavation sequence in the numerical simulation of the CRD method is A-B-C-D. In this section, the tunnel excavated using the A-C-B-D sequence is compared with the tunnel in Section 4.1.

The surface settlement using A-C-B-D sequence excavation is shown in Figure 27, and it can be seen that the surface settlement of each working condition is significantly reduced after using A-C-B-D sequence excavation. The maximum settlement values decreased by 35% for Case 1, 43% for Cases 2 and 3, and 42% for Cases 4 and 5.

Figure 28 shows the displacement of the surrounding rock after excavation using two different excavation sequences. It can be seen that the depth and width of surface settlement are significantly reduced in the case of excavation in the A-C-B-D sequence of excavating the surrounding rock on the submerged side first in Case 4. For tunnels excavated in the A-C-B-D sequence, the width of the surface 2 cm settlement trough is less than double the tunnel width, and the width of the 1 cm settlement trough is about 1.5 times the tunnel width, both of which are less than the settlement of tunnels excavated in the A-C-B-D sequence. This shows that excavating the surrounding rock on one side first and applying support structure can effectively control the surface settlement.

Figure 29 and Table 7 show the settlement values of the surrounding rock after excavation for both excavation sequences. It can be seen that the settlement of the tunnel surrounding rock in the A-C-B-D sequence is better controlled. In Case 1, the maximum settlement value of the surrounding rock decreased by more than 40%, reaching 2.3 cm. The maximum settlement values also decreased by 3.5 cm and 4.4 cm in Case 2 and Case 3, respectively. The overall displacement drop of the surrounding rock in Case 4 is not particularly significant, but the displacement at the left arch shoulder is still controlled to a certain extent. Case 5 is the most unfavorable condition of arch foot dip; after using A-C-B-D sequence excavation, the maximum settlement of tunnel surrounding rock is well controlled, and the overall settlement is reduced by more than 40%.

5. Conclusion

In this paper, numerical simulations of surface water infiltration in shallow buried loess tunnels containing joints in the surrounding rock were carried out to study the mechanical effects of loess tunnels under the influence of joint infiltration, and tunnel excavation simulations under joint infiltration conditions were performed. The following conclusions were drawn:

(1) Large open joints will form a seepage dominant channel when surface water infiltrates, and when the openness gradually increases, surface water will form an instilling effect and quickly form a saturated area in the bottom liner, and the seepage field will change from conical to rectangular. The increase of the number of joints can accelerate the infiltration rate of surface water and form a wider and deeper saturation area.

(2) Under the conditions of uniform surface infiltration and arch top water immersion, which are symmetrically distributed in the infiltration area, the horizontal displacement of the ground and tunnel surrounding rock and lining is not large, and the tunnel is not affected by the bias effect; the surface settlement, settlement trough width, and surrounding rock settlement of arch top water immersion are determined by the width of the water immersion area. Under the condition of arch shoulder submergence, the settlement of arch shoulder on the submerged side increases

significantly, the horizontal displacement of arch waist increases and the horizontal displacement of arch shoulder and arch waist on both sides is asymmetric, and the tunnel is characterized by significant bias force. The most significant effect of wetting on the surface and surrounding rock settlement is on the foot of the tunnel arch, and the surrounding rock and lining of the foot, arch waist, and arch shoulder on the immersed side will produce a large settlement.

(3) CRD method has the advantages of optimizing the lining force and effectively controlling the lining displacement and surrounding rock settlement under various working conditions. The CRD method has no obvious advantage over the three-step method in controlling the vault displacement under the vault flooding condition, but it has good effect in controlling the overall lining displacement. The CRD method can effectively control the settlement of the surrounding rock and reduce the lining under the conditions of waterlogged vault and vault foot, and the settlement of vault and vault shoulder is reduced by 20–30% compared with the three-step method. When using the CRD method of construction, changing the construction sequence can significantly affect the displacement and forces in the surrounding rock [21].

Data Availability

All data and models generated or used during the study are included within the article.

Conflicts of Interest

The authors declare that they have no conflicts of interest.

References

[1] Y. Li, W. Shi, A. Aydin, M. A. Beroya-Eitner, and G. Gao, "Loess genesis and worldwide distribution," *Earth-Science Reviews*, vol. 201, Article ID 102947, 2020.

[2] N. Li and Q. Yang, "Geotechnical engineering problems in water conservancy and civil construction in western China," *Journal of Water Resources and Architectural Engineering*, vol. 17, no. 5, pp. 1–8, 2019.

[3] D. Y. Xie, "Exploration of some new tendencies in research of loess soil mechanics," *Chinese Journal of Geotechnical Engineering*, vol. 23, no. 1, pp. 3–13, 2001.

[4] T. G. Ryashchenko, V. V. Akulova, and M. A. Erbaeva, "Loessial soils of priangaria, transbaikalia, Mongolia, and northwestern China," *Quaternary International*, vol. 179, no. 1, pp. 90–95, 2008.

[5] S. J. Shao, C. Yang, Y. Y. Jiao, and L. si, "Engineering properties of collapsible loess tunnel," *Chinese Journal of Geotechnical Engineering*, vol. 35, no. 9, pp. 1580–1590, 2013.

[6] S. J. Shao, F. Chen, and S. Shao, "Collapse deformation evaluation method of loess tunnel foundation," *Chinese Journal of Rock Mechanics and Engineering*, vol. 36, no. 5, pp. 1289–1300, 2017.

[7] Y. Luo, T. X. Wang, and J. J. Wang, "Finite element seepage flow model for unsaturated loesswith joints," *Journal of Engineering Geology*, vol. 22, no. 6, pp. 1115–1122, 2014.

[8] K. Y. Zhao, Q. Xu, and F. Z. Liu, "Seepage characteristics of preferential flow in loess," *Chinese Journal of Geotechnical Engineering*, vol. 42, no. 5, pp. 941–650, 2020.

[9] X. H. Deng, W. P. Cao, and D. S. Yang, "Stability analysis of shallow loess tunnel considering rainfall infiltration," *Journal of Civil & Environmental Engineering*, vol. 42, no. 2, pp. 45–55, 2020.

[10] Y. H. Zhao, H. Y. Luo, and X. Y. Miao, "Research on the characteristics of steel arch stress and variation of water content of loess tunnel surrounding rock," *Railway Standard Design*, vol. 63, no. 4, pp. 128–131, 2019.

[11] W. L. Zhao, H. P. Lai, and Y. Y. Liu, "Analysis of lining cracking of loess highway tunnel under flooded surrounding rock conditions," *China Journal of Highway and Transport*, vol. 31, no. 5, pp. 117–126, 2018.

[12] E. Wang, Q. G. Liang, and F. Wang, "Study on the influence of different flooding methods onthe deformation of loess metro tunnel," *Journal of Railway Science and Engineering*, vol. 1, no. 15, pp. 156–162, 2018.

[13] S. Xue, D. S. Yang, and X. H. Deng, "Influence of surface water infiltration on stability of shallow buried loess tunnel," *Journal of Xi'an Technological University*, vol. 37, no. 8, pp. 600–606, 2017.

[14] Y. B. Li, C. H. Zhu, and Y. Duan, "Mechanical response of lining structure under wetting effect of surrounding soil in loess tunnel," *Journal of Water Resources and Architectural Engineering*, vol. 18, no. 6, pp. 33–38, 2020.

[15] C. Gong and W. Ding, "A computational framework to predict the water-leakage pressure of segmental joints in underwater shield tunnels using an advanced finite element method," *International Journal for Numerical and Analytical Methods in Geomechanics*, vol. 42, no. 16, pp. 1957–1975, 2018.

[16] M. Lei, B. Zhu, C. Gong, W. Ding, and L. Liu, "Sealing performance of a precast tunnel gasketed joint under high hydrostatic pressures: site investigation and detailed numerical modeling," *Tunnelling and Underground Space Technology*, vol. 115, Article ID 104082, 2021.

[17] C. Gong, W. Ding, K. Soga, K. M. Mosalam, and Y. Tuo, "Sealant behavior of gasketed segmental joints in shield tunnels: an experimental and numerical study," *Tunnelling and Underground Space Technology*, vol. 77, pp. 127–141, 2018.

[18] C. Gong, W. Ding, K. M. Mosalam, S. Günay, and K. Soga, "Comparison of the structural behavior of reinforced concrete and steel fiber reinforced concrete tunnel segmental joints," *Tunnelling and Underground Space Technology*, vol. 68, pp. 38–57, 2017.

[19] C. Gong, W. Ding, and D. Xie, "Parametric investigation on the sealant behavior of tunnel segmental joints under water pressurization," *Tunnelling and Underground Space Technology*, vol. 97, Article ID 103231, 2020.

[20] C. Gong, W. Ding, K. Soga, and K. M. Mosalam, "Failure mechanism of joint waterproofing in precast segmental tunnel linings," *Tunnelling and Underground Space Technology*, vol. 84, pp. 334–352, 2019.

[21] W. Ding, C. Gong, K. M. Mosalam, and K. Soga, "Development and application of the integrated sealant test apparatus for sealing gaskets in tunnel segmental joints," *Tunnelling and Underground Space Technology*, vol. 63, pp. 54–68, 2017.

[22] B. X. Yuan, Z. J. Li, W. J. Chen et al., "Influence of groundwater depth on pile–soil mechanical properties and

fractal characteristics under cyclic loading," *Fractal and Fractional*, vol. 6, no. 4, p. 198, 2022.

[23] B. X. Yuan, Z. H. Li, Y. M. Chen et al., "Mechanical and microstructural properties of recycling granite residual soil reinforced with glass fiber and liquid-modified polyvinyl alcohol polymer," *Chemosphere*, vol. 286, no. 1, Article ID 131652, 2022.

[24] J. Q. Dang and J. Li, "The structural strength and shear strength of unsaturated loess," *Journal of Hydraulic Engineering*, vol. 7, pp. 79–83, 2001.

[25] M. H. Zhang, Y. L. Xie, and B .J Liu, "Analysis of the shear strength characteristics of loess during moisture increase," *Rock and Soil Mechanics*, vol. 27, no. 7, pp. 1195–1200, 2006.